12-20-2002

He II Reverberation in Active Galactic Nucleus Spectra

Mark C. Bottorff
Southwestern University

Jack A. Baldwin
Michigan State University

Gary J. Ferland
University of Kentucky, gary@uky.edu

Jason W. Ferguson
Wichita State University

Kirk T. Korista
Western Michigan University

The Astrophysical Journal, 581:932–947, 2002 December 20

He II REVERBERATION IN ACTIVE GALACTIC NUCLEUS SPECTRA

Mark C. Bottorff
Physics Department, Southwestern University, Georgetown, TX 78627-0770

Jack A. Baldwin
Department of Physics and Astronomy, Michigan State University, East Lansing, MI 48824-1116

Gary J. Ferland
Physics Department, University of Kentucky, Lexington, KY 40506

Jason W. Ferguson
Department of Physics, Wichita State University, Wichita, KS 67260-0032

and

Kirk T. Korista
Physics Department, Western Michigan University, Kalamazoo, MI 49008
Received 2002 May 20; accepted 2002 August 26

ABSTRACT

This paper compares the observed reverberation response lags and the intensity ratios of the broad-line region (BLR) emission lines He II λ1640, He II λ4686, and C IV λ1549 with predictions. Published observations indicate that the He II λ1640 lag is 3 times shorter than the lags of He II λ4686 or C IV λ1549. Diverse models, however, do not reproduce this observation. Extensive improved numerical simulations of the hydrogenic isoelectronic sequence emission show that the He II spectrum remains especially simple, even in the central regions of a luminous quasar. Line trapping never builds up a significant population of excited states, and the emissivities of the two He II lines are close to simple case B predictions. Using improved He II calculations, we computed the lags of distributions of clouds concentrated in approximate radius-dependent pressure laws as well as the lags of locally optimally emitting cloud (LOC) distributions. In addition, the effect on lags and intensities due to anisotropic beaming of line emission and observer orientation angle with respect to an obscuring disk is estimated. Comparing our results to observations, we do not see how *any* distribution of clouds can produce intrinsic He II λ1640 and He II λ4686 emission with substantially different responses, nor do we see how He II λ1640 can vary on a substantially shorter timescale than C IV λ1549. Our models suggest that in fact the observed He II λ1640 reverberation timescale is shorter than expected rather than the observed He II λ4686 timescale being longer than expected. We discuss a possible explanation.

Subject headings: galaxies: active — galaxies: nuclei — galaxies: Seyfert

On-line material: color figure

1. INTRODUCTION

The past decade has seen a revolution in our understanding of the emission-line regions of AGNs due to extensive line continuum reverberation studies (see Peterson 2001 for a brief review of reverberation mapping applied to AGNs). These have shown that the emitting gas is distributed over a wide range of radii and ionization, with significant stratification between species of different ionization potentials. The broad-line region (BLR) is obviously much more complex than early models that used a single representative cloud at some characteristic radius and density as the basis of studies of BLR properties.

The atomic physics of many of the species present in the BLR is well understood, and it should be straightforward to predict the reverberation behavior of many emission lines. The He^+ ion is a particularly simple case. The atomic processes are very well documented, and as we will show below, a clear expectation is that the He II λ1640 and λ4686 lines should vary in lockstep with no significant time lag between them. The C IV λ1549 line is also produced in a simple situation, and as we will show below, most BLR models predict that the He^+ and C^{3+} ions should coexist closely enough that there should be no more than a modest difference in their reverberation time lags.

Yet in all cases in which the He II λ1640 and C IV λ1549 lag times have both been measured in the same object, it is found that the He II line varies on a much shorter timescale than C IV. In the one object where both He II λ1640 and λ4686 have been measured, the two lines also may vary with significantly different timescales. This paper explores this conundrum.

We first review the reliability of the observations and then discuss the basic simplicity of the He^+ ion. Most of this paper is then devoted to working through the predicted reverberation behavior of He II and C IV lines in a range of models that spans the most frequently suggested structures of the BLR to see if subtle details can lead to the observed differences in the lag times in spite of the underlying atomic simplicity. Finally, we will offer our best guess at what has been overlooked in the reverberation analysis and must be included in the future in order to explain the observed lag differences.

2. THE OBSERVATIONAL SITUATION: He II AND C IV REVERBERATION

We are interested in both the relative intensities and lag times between different He II lines (λ1640 and λ4686) and

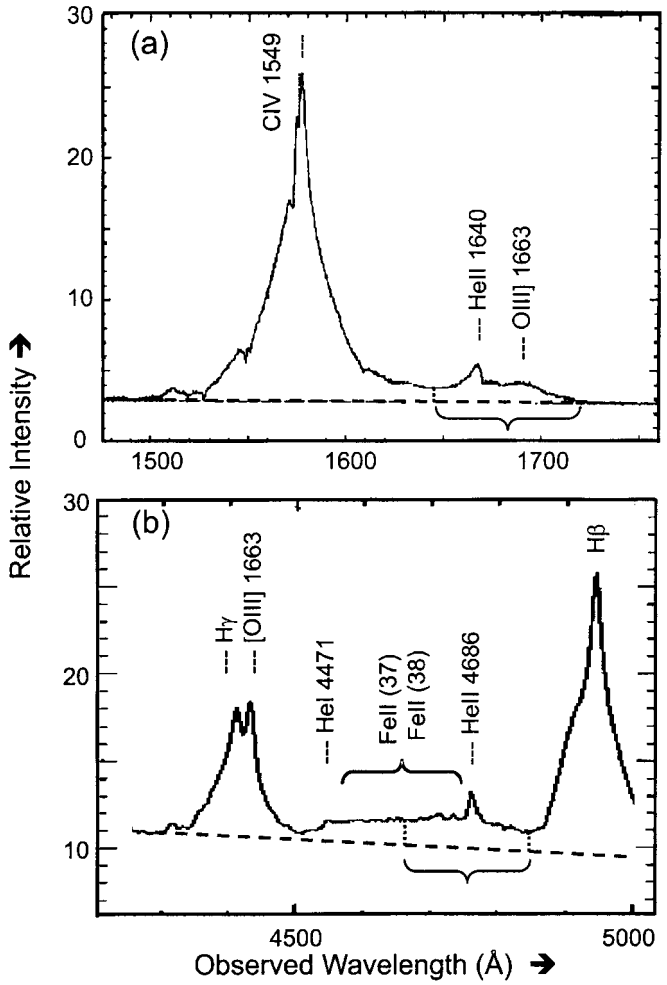

FIG. 1.—Regions around He II λ1640 and He II λ4686 in the spectrum of NGC 5548, on the same velocity scale. Data are from, respectively, K95 and D93. The dashed lines show the approximate continuum level, and the heavy brackets below the continuum show the areas included in the λ4686 and λ1640 flux measurements.

the lag time of the He II lines relative to lines of other species.

NGC 5548 is by far the best studied AGN, with major optical/UV spectroscopic monitoring campaigns in 1989 (Clavel et al. 1991, hereafter C91; Dietrich et al. 1993, hereafter D93) and then again in 1993 (Korista et al. 1995, hereafter K95). It is also the only object for which λ1640 and λ4686 have both been measured in the same campaigns. In an early study, Wamsteker et al. (1990, hereafter W90) measured these two He II lines from contemporaneous *IUE* and ground-based observations of modest signal-to-noise ratio (S/N) and spectral resolution spanning 1978–1986 in 29 epochs. Both lines are blended with nearby lines of comparable and much greater strength. He II λ1640 is blended with O III] λλ1661, 1666, the red wing of C IV λ1549, and perhaps Al II λ1670 and emission of uncertain origin near 1600 Å (rest-frame). He II λ4686 is blended with optical Fe II (multiplets 37 and 38 and others) and the blue wing of Hβ. Figure 1 illustrates each line's observed frame spectral regions in representative mean spectra—from the 1993 *Hubble Space Telescope* (*HST*)/ground campaign (K95) for λ1640 and from the 1989 *IUE*/ground campaign (C91; D93) for λ4686.

After deblending as best they could the λ1640 and λ4686 lines from the surrounding contaminating emission, removing the narrow-line region contributions to the two lines, and correcting the spectra for Galactic foreground extinction [assuming $R = 3.1$, $E(B-V) = 0.05$], W90 found the broad-line flux ratio $f(\lambda1640)/f(\lambda4686)$ to have a mean value of 6.9 ± 3.4, which agrees well with the expected recombination value of 6–8 that we will discuss below. However, their results also suggested that this ratio *varied* from 4 to 10 during the time span of their observations, which if true would indicate different lag times for the two He II lines.

Further measurements covering both the λ1640 and λ4686 lines in NGC 5548 were made by the AGN Watch group in a 280 day *IUE*/ground campaign in 1989 (C91; D93). Dumont, Collin-Souffrin, & Nazarova (1998) compared the individual measurements of "λ1640" and "λ4686" from the 1989 campaign for 16 nearly simultaneous observations and reported ratios that varied from 0.589 to 4.26 with a mean ratio of 2.18 ± 1.22 (their inferred mean broad-line spectrum yielded a ratio of 3.15). However, C91 and D93 caution that blending contaminates the measurements of both of these lines. Narrow emission lines, reddening, and (probably in the 1989 *IUE* data) detector nonlinearities are also relevant. When we make our best guesses at the appropriate corrections for these effects (see the Appendix), we find that the mean intensity ratio is more likely be about 5, much closer to the recombination value. Table 1 summarizes the relevant line intensity measure-

TABLE 1
OBSERVED FLUX AND RATIOS FOR NGC 5548

Line	Flux ($\times10^{-14}$ ergs cm^{-2} s^{-1})[a]	Line Ratio	Line Ratio Value
1989 Campaign:			
He II λ1640[b]	86 ± 30%	C IV λ1549/He II λ1640	9.3 ± 3.0
He II λ4686	17 ± 50%	He II λ1640/He II λ4686	5.1 ± 3.0
C IV λ1549	797 ± 10%	C IV λ1549/He II λ4686	48 ± 24
1993 Campaign:			
He II λ1640[b]	78 ± 20%	C IV λ1549/He II λ1640	9.7 ± 2.1
C IV λ1549	757 ± 10%		

[a] In the observed frame, corrected for narrow emission component and dereddened for the Galaxy; $R = 3.1$, $E(B-V) = 0.03$.

[b] After subtracting of 33% of the He III + O III] blend to account for O III] strength and applying other corrections to 1989 data as described in the Appendix.

TABLE 2
OBSERVED TIME LAGS AND RATIOS FOR NGC 5548

Line	Lag (days)	Lag Ratio	Lag Ratio Value
1989 Campaign:			
He II λ1640+O III]1663	$3.0^{+2.9}_{-1.1}$	C IV λ1549/He II λ1640+O III]	$3.2^{+3.2}_{-1.8}$
He II λ4686	$8.5^{+3.4}_{-3.4}$	He II λ1640/He II λ4686	$0.4^{+1.0}_{-0.2}$
C IV λ1549	$9.5^{+2.6}_{-1.0}$	C IV λ1549/He II λ4686	$1.1^{+1.3}_{-0.4}$
1993 Campaign:			
He II λ1640+O III] λ1663	$2.0^{+0.3}_{-0.4}$	C IV λ1549/He II λ1640+O III]	$3.4^{+1.5}_{-0.9}$
C IV λ1549	$6.8^{+1.1}_{-1.1}$		

ments from the 1989 campaign with these corrections included and also shows results for C IV λ1549 and He II λ1640 from the 1993 campaign (He II λ4686 was not measured in the latter campaign).

However, C91 and D93 may have found substantially different lag times for λ1640 and λ4686 during the 1989 campaign. The most carefully measured values of these lags in the 1989 data are $3.0^{+2.9}_{-1.1}$ days for the λ1640 blend and $8.5^{+3.4}_{-3.4}$ days for the λ4686 blend, as determined over the full 280 day campaign (Peterson & Wandel 1999). In addition, both the 1989 and 1993 campaigns found that He II λ1640 varied much more rapidly than the adjacent C IV λ1549 line (C91; K95).

These lag times are listed in Table 2. The first two columns show the centroid of the lag (in days) of the cross-correlation function of the observed emission-line light curves for He II λ1640, He II λ4686, and C IV λ1549 with the light curve of the observed continuum at 1350 Å as determined from the 1989 and 1993 observing campaigns. The error bars on the lag values are from Peterson & Wandel (1999). The last two columns give line lag ratios. The (estimated) error bars on the lags are not symmetric, with the uncertainty in the longer lag direction often being larger than in the shorter lag direction. We used a simple square or boxcar uniform distribution of errors. The resulting uncertainty in the lags is conservative since it puts extra weight on the endpoints of the distribution.

Again, blending with other emission lines is a major source of uncertainty not included in calculating the observed lags or the error bars. All measurements of the He II λ1640 lags in this and other Seyfert 1 AGNs have included the light of O III] λλ1661, 1666 and perhaps other weaker contributions. The λ4686 measurement window (see Fig. 1) probably contained a larger contribution from contaminating—and more slowly varying—emission. In addition, the formal error bars on the two lags indicate that they may well be consistent with one another, bearing in mind too that the sampling intervals for these two lines were 4 days for the UV line and typically, though unevenly, 1 week for the optical line. However, there is clearly *something* varying at or very near the wavelengths of these two helium lines in the spectrum of NGC 5548, and the best estimate of the lag times is that the λ1640 feature varies 3 times more rapidly than λ4686. In this case the intensity ratio of these lines should also change with time, as has been reported by W90.

The ratio of the He II λ1640 and C IV λ1549 lines is also known for several additional AGNs. Table 3 compiles results for all of the objects for which there are reliable lag measurements of both lines. The trend is clear. The He II λ1640 lag times are measured to be several times shorter than those of C IV λ1549. This difference has been accepted without much comment because He^+ has a significantly higher ionization potential than C^{3+}, and the results from other emission lines show a clear trend of shorter lag times with higher ionization potential. Despite the substantial uncertainties on individual objects and campaigns, all studies show a ratio of lags that is substantially larger than unity, suggesting that this is a true property of these AGNs.

3. THE THEORETICAL He II SPECTRUM

We have carefully modeled the He^+ atomic structure for the calculations presented here. Photoionized models were computed using the development version of the radiative equilibrium code CLOUDY, last described by Ferland (2002).[1] This includes many recent improvements to the portions of the code that predict the intensities of hydrogen and the hydrogen ion–like isoelectronic sequence. Ferguson & Ferland (1997) and Ferguson et al. (2001) describe the model of the hydrogen-like isoelectronic sequence, which includes He II, the focus of this paper. These show that the predictions agree with the more extensive calculations of Storey & Hummer (1995) to better than 5% for much lower densities than are considered here. The model atom includes all collisional and radiative effects, including pumping by the continuum and line overlap, collisional excitation and ionization, and line trapping.

We used the continuum shape deduced by Dumont et al. (1998) for NGC 5548 and a solar composition. For simplicity, the hydrogen density was taken to be constant within each cloud, with a column density of 10^{23} cm^{-2}.

[1] Ferland (2002) is available at http://nimbus.pa.uky.edu/cloudy.

TABLE 3
LAG(C IV λ1549)/LAG(He II λ1640) IN VARIOUS OBJECTS

Object	lag(1549)/lag(1640)[a]	References
NGC 5448.....	3.3	Average of Table 2 values
NGC 3783.....	5.0	Reichert et al. 1994
Fairall 9	3.4	Rodriguez-Pascual et al. 1997
NGC 7469.....	2.4	Wanders et al. 1997
3C 390.3.....	3.8	O'Brien et al. 1998
Average.....	3.6	

[a] Calculated from peaks of cross-correlation functions. For NGC 3783, the GEX measurement was used.

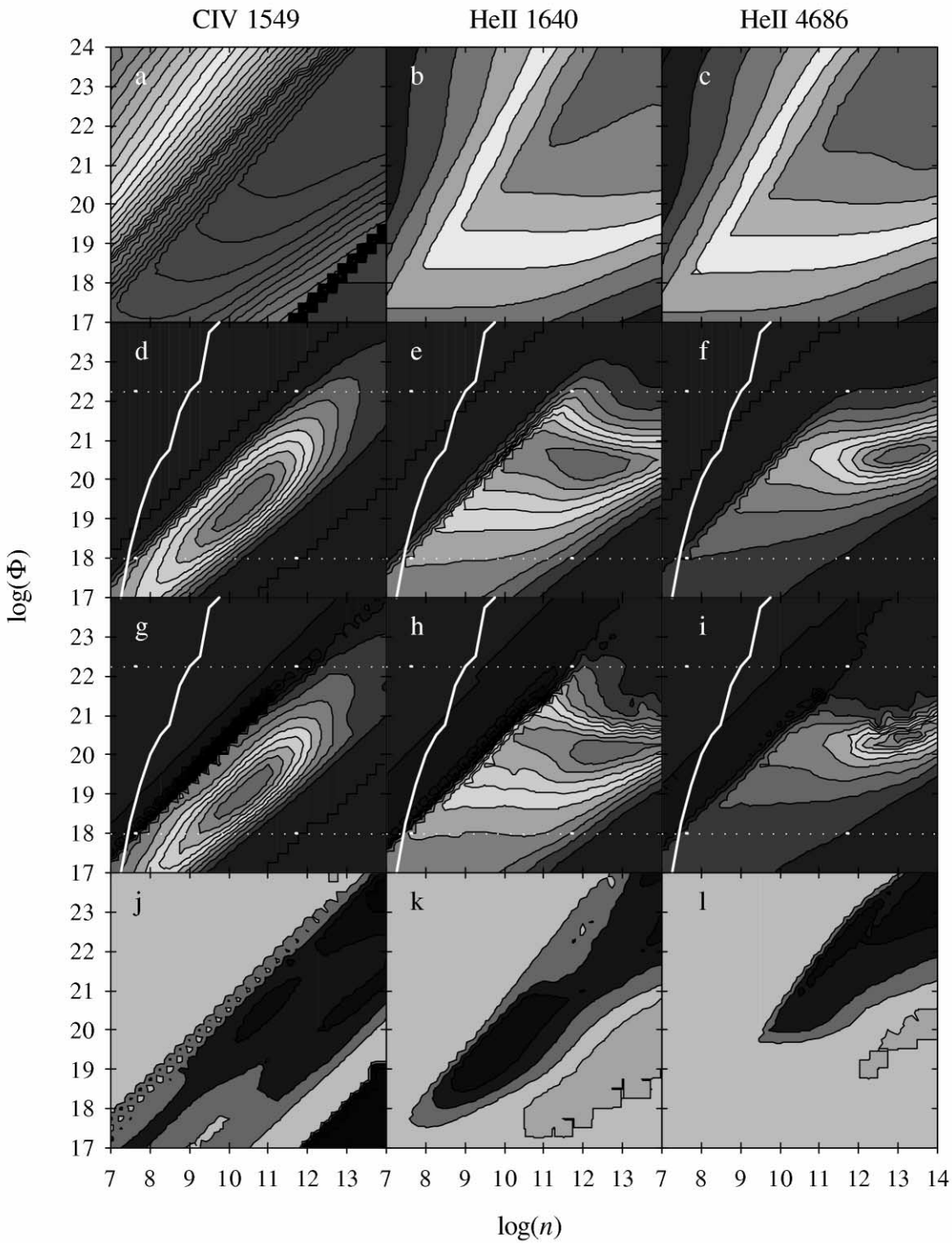

FIG. 2.—(*a*)–(*c*) log of the total (front-side plus back-side) emission-line flux F emergent from 10^{23} cm^{-2} column density clouds normalized by the maximum F for C IV λ1549, He II λ1640, and He II λ4686, respectively, as a function of $\log n$ and $\log \Phi$. The contours are 1 dex. (*d*)–(*f*) On a linear scale, the emission-line flux weighted by the covering factor for the optimal LOC model ($\gamma = -1.2$, $\delta = -1.0$), corrected for the $\log n - \log \Phi$ grid and normalized to the maximum value on the grid. (*g*)–(*i*) Also on a linear scale, the optimal LOC model weighting of $\partial F/\partial \Phi$ for the responsivity-weighted radius, normalized to the maximum on the grid. In (*d*)–(*i*) the contours are in steps of 0.1, the region to the left of the jagged near vertical line shows where the recombination time is longer than 1 day, and the horizontal dashed lines show the limits of $\log \Phi$ integration for our models. Note the similarity between (*d*)–(*f*) and (*g*)–(*i*). (*j*)–(*l*) Relative flux emergent from the dark sides of the clouds (h_D). Lighter areas corresponds to emission isotropy $h_D = 0.5$. Darker areas correspond to higher anisotropy (lower h_D). Contours are in steps of 0.1. [*See the electronic edition of the Journal for a color version of this figure.*]

Figures 2*a*, 2*b*, and 2*c* show for C IV λ1549, He II λ1640, and He II λ4686, respectively, the predicted total emission-line flux, each normalized to its maximum value, as a function of density n (in units of cm^{-3}) and ionizing radiation flux Φ (in units of cm^{-2} s^{-1}), from one-dimensional slab clouds of column density 10^{23} cm^{-2}. Contours are logarithmically spaced at 1 dex intervals. Calculations were carried out on a uniformly spaced (0.25 dex) grid in the $\log n$ versus

log Φ plane. The distributions of He II line emissivities are different from the "peaky" collisionally excited C IV λ1549 line. These figures show that the predicted intensities of the He II lines are comparatively insensitive to assumed details.

The emission planes shown in Figures 2*a*–2*c* illustrate the global properties of all possible clouds. The observed spectrum is obtained by integrating over the distribution of the subset of clouds that actually exist. In this work we describe the integration in terms of weighting functions that are power-law distribution functions in n and R (the locally optimally emitting cloud [LOC] model of Baldwin et al. 1995 and the pressure-law models in Goad, O'Brien, & Gondhalekar 1993, respectively).

An example of such weighting is the LOC model presented by Korista & Goad (2000, hereafter KG00). This model was chosen from a range of simple LOC models that fit the mean emission-line strengths of the stronger UV emission lines of the 1993 *HST* campaign, with weighting parameters that would produce a wide spread in the lags of the emission lines without exceeding limitations in covering fraction. Figures 2*d*–2*f* show the expected emissivity for this model as a function of n and Φ. These are the result of multiplying Figures 2*a*–2*c* by the weighting functions in KG00. In each figure the flux is normalized to its maximum, and the contours are now shown on a *linear* scale with intervals of 0.10. Emission from the He II lines remains considerably spread out in the log n–log Φ plane compared to C IV λ1549.

Three regions are present in Figures 2*d*–2*f*. The declining emission above and to the left of the diagonal from the low- to high Φ-n corners corresponds to the coronal phase, where the gas is very highly ionized and produces little UV/optical emission. Temperatures in this region typically lie near 10^6 K (see Fig. 2 of Korista et al. 1997). Below and to the right of this diagonal, gas is in the nebular phase and temperatures are near 10^4 K. The equivalent widths of the He II lines change very little in this second region. He II lines form primarily by recombination, so they track the He^{++} fraction of the cloud, and their emissivity has weak temperature dependence ($j \sim T^{-1}$). The size of the He II–emitting region inside each individual cloud, which governs the intensity of the He II recombination lines, is determined almost entirely by the shape of the ionizing continuum rather than by cloud parameters and is in fact a primary stellar temperature indicator for planetary nebulae (Osterbrock 1989). Finally, in the lower right-hand corner of each box there is a region with no emissivity because the weighting functions preclude having any gas with these n-Φ values.

Figure 3 shows the He II λ1640/He II λ4686 intensity ratio across the log n–log Φ plane. The ratio is large in the coronal phase because of both the high temperature and the influence of line pumping by the incident continuum. However, Figure 2 shows that this gas has very small emissivity and can contribute little to the observed lines. The He II λ1640/He II λ4686 flux ratio falls to 3–4 in the region within the density-flux plane where these lines have their peak emissivities (log $n \sim 13$, log Φ ∼ 21). However, this region is comparatively small and emits very little else. Calculations below show that when the emission is integrated over models that predict the other lines, the intensity ratio He II λ1640/He II λ4686 is in the range 6–8. Thus, over most of the region where there is significant emission from the other lines, such as C IV (compare to Figs. 2*d*–2*f*), the most dominate physical situation remains close to the case B recombination value, ∼9 (Storey & Hummer 1995).

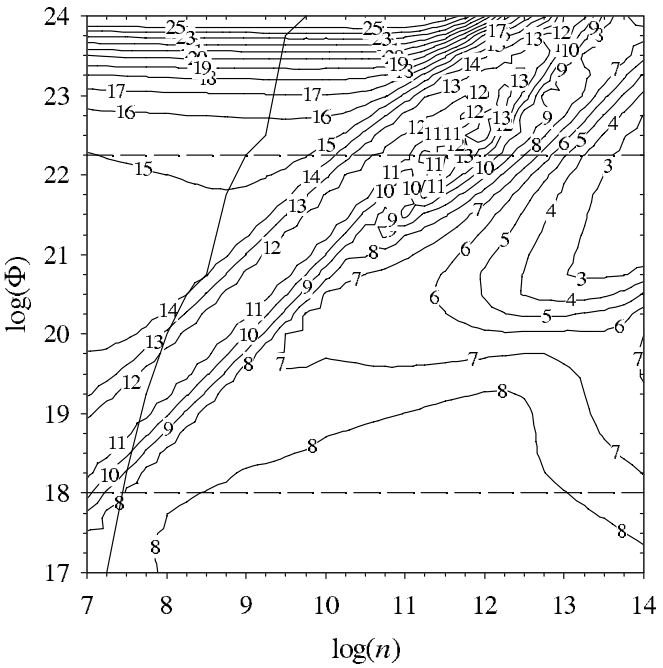

FIG. 3.—Intensity of He II λ1640 relative to He II λ4686. The ratio is greater than 10 in regions that are highly ionized, the He II lines are optically thin, and continuum pumping of the UV lines is efficient. The lines are very weak in these cases (see Fig. 2). Over most parameters where the lines have significant equivalent width the intensity ratio lies between 7 and 9 and are close to the case B predictions of Storey & Hummer (1995). The jagged near-vertical line shows where the recombination time is longer than 1 day, and the horizontal dashed lines show the limits of log Φ integration for our models.

He II emission remains very simple because the atom's resonance lines are effectively destroyed by a combination of Bowen O III fluorescence (Weymann & Williams 1969) and photoionization of hydrogen in the ground state (MacAlpine 1981). These calculations confirm the long-held suspicion that the He II λ1640/He II λ4686 ratio remains close to its optically thin case B ratio (MacAlpine 1981; MacAlpine et al. 1985). The He II recombination lines remain optically thin for most conditions where strong lines form. This simplicity makes the He II spectrum a powerful emission-line tool—the simulations show that the spectrum should be relatively model independent.

4. EMISSION-LINE INTENSITY AND REVERBERATION

In this section we present general expressions for the total line intensity I and the response-weighted radius R_{RW} at which an emission line is formed in terms of integrations over the variables log n and log Φ. These are needed because I and R_{RW} are measurable quantities, while n and Φ are the physical parameters that we use to describe the distributed geometry required by the reverberation results.

4.1. *Observed Line Intensity*

The observed BLR line intensity is calculated by integrating the differential intensity (the intensity directed toward the observer per unit volume) over the volume of the BLR.

Thus, we have

$$I = \int_{\rm BLR} (jh) dV \ , \tag{1}$$

where dV is a volume element and the differential intensity per unit volume is symbolized by (jh). It is written as the product of two functions to separate the total integrated emission power per unit volume (j, in units of ergs cm^{-3} s^{-1}) from the portion of the integrated emission power beamed toward the observer per unit area per steradian (h, in units of cm^{-2} sr^{-1}). The function h depends on μ, the cosine of the angle between the position vector relative to the continuum source, and a unit vector directed from the observer toward the continuum source. This choice puts into h geometric effects such as anisotropic beaming or obscuration by a thick disk. By using this convention, j can be estimated from one-dimensional photoionization codes like CLOUDY, and analytical models may be employed for h. Since emission may arise from an ensemble of clouds of different densities, we write j as

$$j \propto \int_{n_1}^{n_2} F(n, \Phi) \frac{\partial^2 C}{\partial n \partial R} dn \ , \tag{2}$$

where F (in units of ergs cm^{-2} s^{-1}) is the line emission from a cloud with particle density n exposed to ionizing flux Φ, per unit area of cloud surface, and $\partial^2 C/\partial n \partial R$ is the differential covering fraction of BLR clouds at radius R as seen from the continuum. The limits of integration range from the smallest cloud density n_1 to the largest n_2. Substituting equation (2) into equation (1) gives

$$I = \int_{\rm BLR} \int_{n_1}^{n_2} F(n, \Phi) \frac{\partial^2 C}{\partial n \partial R} h \, dn \, dV \ . \tag{3}$$

We will calculate I for several spherically symmetric isotropic emission models using a grid of uniformly spaced photoionization calculations in $\log n$ and $\log \Phi$. Thus, h is constant, and the volume element is $4\pi R^2 \, dR$. It is advantageous to change the integration variables from R and n to $\log n$ and $\log \Phi$. Since $\Phi = L_c/4\pi R^2$, we have $R \propto \Phi^{-1/2}$ and $dR \propto \Phi^{-3/2} \, d\Phi$. Next changing variables from n and Φ to $\log n$ and $\log \Phi$ gives $dn \propto n \, d \log n$ and $d\Phi \propto \Phi \, d \log \Phi$, so we have

$$I \propto \int_{\log \Phi_1}^{\log \Phi_2} \int_{\log n_1}^{\log n_2} F(n, \Phi) \frac{\partial^2 C}{\partial n \partial R} \Phi^{-3/2} n \, d \log n \, d \log \Phi \ , \tag{4}$$

where Φ_1 and Φ_2 are the ionizing continuum flux at the maximum radius $R_{\rm max}$ (minimum flux) and the minimum integration radius $R_{\rm min}$ (maximum flux), respectively. $R_{\rm min}$ is taken to be where the gas becomes thermalized and, after weighting by the covering factor and including the effect of geometry, no longer emits significant line radiation. The radius $R_{\rm max}$ is taken to be where line emission is truncated because of the onset of dust. We explicitly leave $\partial^2 C/\partial n \partial R$ untransformed for easy substitution of its functional forms in § 5.

4.2. *The Responsivity-Weighted Radius*

The responsivity-weighted radius ($R_{\rm RW}$) represents the characteristic radial distance from the continuum source to the gas emitting the line in question (Goad et al. 1993). We use a form of $R_{\rm RW}$ that includes anisotropic beaming. It is given by

$$R_{\rm RW} = \frac{\int_{\rm BLR} \eta(jh) R(1+\mu) \, dV}{\int_{\rm BLR} \eta(jh) \, dV} \ . \tag{5}$$

The quantity η in equation (5) is called the responsivity and is defined by

$$\eta \equiv \frac{\delta(jh)}{(jh)} \frac{\Phi_0}{\delta \Phi} = \frac{\partial (jh)}{\partial \Phi} \frac{\Phi_0}{(jh)} \ . \tag{6}$$

The quantity $\delta(jh)$ represents an infinitesimal change in (jh) due to an infinitesimal change $\delta\Phi$ in the ionizing continuum flux from a value Φ_0. For model calculations, Φ_0 is usually taken to be the mean ionizing continuum flux. Since it is assumed that $\Phi_0 \propto L_c$, where L_c is the mean continuum luminosity, equation (6) may also be written as $\eta = [\delta(jh)/(jh)](L_c/\delta L_c)$ or, in the case in which there is a unique cloud particle density at each radius, $\eta = [\delta(jh)/(jh)](U_c/\delta U_c)$, where U_c is the ionization parameter, defined by $U_c = L_c/4\pi R^2 nc$, where n is the cloud total hydrogen density at radius R and c is the speed of light (Goad et al. 1993).

The $R_{\rm RW}$ measures the time lag between *changes* of the ionizing continuum and changes in an emission line. As a result, it may be compared to observations. Physically, $R_{\rm RW}$ is the characteristic radius at which the response of line-emitting gas to temporal changes of the continuum, smeared by light-travel time delays, is manifested. The $R_{\rm RW}$ for each emission line will differ because different lines form at different places on the $\log n$–$\log \Phi$ plane. Alternatively, any two lines that are formed under similar ionization conditions will have similar $R_{\rm RW}$.

We estimate the effects of nonconstant h in § 6. Here we calculate $R_{\rm RW}$ when h is a constant and j depends only on R. This means that the emission from clouds is isotropic. The assumption simplifies our work and allows us to compare our general definition of $R_{\rm RW}$ with the results in Goad et al. (1993). Using spherical coordinates, equation (5) becomes

$$R_{\rm RW} = \frac{\int_{R_{\rm min}}^{R_{\rm max}} \eta j 4\pi R^2 \, dR}{\int_{R_{\rm min}}^{R_{\rm max}} \eta j 4\pi R^2 \, dR} = \frac{\int_{R_{\rm min}}^{R_{\rm max}} \eta L(R) R \, dR}{\int_{R_{\rm min}}^{R_{\rm max}} \eta L(R) \, dR} \ , \tag{7}$$

where the radial limits of integration are defined in § 4.1 and $L(R) = j4\pi R^2$ is the differential line luminosity in a thin shell of radius R. The last expression in equation (7) is exactly the same as in Goad et al. (1993). Since h is set equal to a constant, equation (6) becomes

$$\eta \equiv \frac{\partial j}{\partial \Phi} \frac{\Phi_0}{j} \ . \tag{8}$$

Substitution into equation (7) gives

$$R_{\rm RW} = \frac{\int_{R_{\rm min}}^{R_{\rm max}} (\partial j/\partial \Phi) R \, dR}{\int_{R_{\rm min}}^{R_{\rm max}} (\partial j/\partial \Phi) \, dR} \ , \tag{9}$$

where we have used the fact that $4\pi R^2 \Phi_0 = L_c$ is independent of R and so the combination may be removed from the integrands of each integral and cancelled. Thus, for isotropic emission, $R_{\rm RW}$ is the expected value of R weighted by $\partial j/\partial \Phi$. Substituting equation (2) into equation (9) and taking the operator $\partial/\partial\Phi$ inside the integral over n gives

$$R_{\rm RW} = \frac{\int_{R_{\rm min}}^{R_{\rm max}} \int_{n_1}^{n_2} (\partial F/\partial \Phi)(\partial^2 C/\partial n \partial R) R \, dn \, dR}{\int_{R_{\rm min}}^{R_{\rm max}} \int_{n_1}^{n_2} (\partial F/\partial \Phi)(\partial^2 C/\partial n \partial R) \, dn \, dR} \ . \tag{10}$$

We will calculate $R_{\rm RW}$ for several isotropic emission models using a grid of uniformly spaced photoionization calculations in $\log n$ and $\log \Phi_0$. As with the formula for intensity (eq. [4]), it is advantageous to change the integration variables from R and n to $\log n$ and $\log \Phi_0$. Note that we have considered R and Φ as independent quantities because of the dependence of Φ on the time-dependent continuum L_c. The quantity $\partial F/\partial \Phi$ is evaluated at fixed (in time) flux Φ_0 and may be traced back to the assumption that emissivity is a linear function of Φ (see Blandford & McKee 1982). Making the same change of variables that leads to equation (4) gives

$$R_{\rm RW} \propto \frac{\int_{\log \Phi_1}^{\log \Phi_2} \int_{\log n_1}^{\log n_2} (\partial F/\partial \Phi)(\partial^2 C/\partial n \partial R)\Phi^{-1} n \, d\log n \, d\log \Phi}{\int_{\log \Phi_1}^{\log \Phi_2} \int_{\log n_1}^{\log n_2} (\partial F/\partial \Phi)(\partial^2 C/\partial n \partial R)\Phi^{-1/2} n \, d\log n \, d\log \Phi} . \quad (11)$$

Both $\partial F/\partial \Phi$ and $\partial^2 C/\partial n \partial R$ are untransformed for easy insertion of photoionization calculations and different covering fraction formulae.

The formula for $R_{\rm RW}$ (eq. [11]) involves $\partial F/\partial \Phi$. For numerical calculations of equation (11), the derivative at each grid point was computed numerically by calculating an additional photoionization grid offset -0.05 dex in $\log \Phi$ from the previous grid and a using a simple first-order finite difference scheme. Thus, we have

$$\frac{\partial F}{\partial \Phi} \approx \frac{F(n, \Phi) - F(n, \Phi 10^{-0.05})}{\Phi - \Phi 10^{-0.05}} . \quad (12)$$

The derivative approximation in equation (12) is weighted by $\partial^2 C/\partial n \partial R$ and inserted into equation (11). Different $\partial^2 C/\partial n \partial R$ values are described in §§ 5.2 and 5.3, and the corresponding ratios of I and $R_{\rm RW}$ for He II λ1640, He II λ4686, and C IV λ1549 are calculated.

5. THE EFFECT OF BLR CLOUD DISTRIBUTIONS ON REVERBERATION RESULTS

We now take the formalism developed above for determining I and $R_{\rm RW}$ and insert different BLR cloud distributions that span the range of what are currently considered to be realistic models. At one extreme is the very simple, but ad hoc, picture in which the gas is distributed according to a radius-dependent pressure law that is a free parameter (Rees, Netzer, & Ferland 1989; Goad et al. 1993; Kaspi & Netzer 1999). At the opposite end of the range is the LOC model, in which the clouds have a wide distribution of properties at every radius, but the powerful selection effects introduced by atomic and plasma physics determine the integrated BLR spectrum. It has been shown that in the latter case the overall emitted spectrum is very similar to typical AGN spectra independent of the detailed structure of the BLR (Baldwin et al. 1995; Korista et al. 1997). KG00 used an LOC model to describe the mean UV broad emission line spectrum of NGC 5548.

We use these models to see whether it is possible, over this wide range of parameter space, to produce $R_{\rm RW}$(He II λ1640)/$R_{\rm RW}$(He II λ4686) and $R_{\rm RW}$(C IV λ1549)/$R_{\rm RW}$(He II λ1640) values that are consistent with the observed lag ratios. Throughout this section we assume that the BLR geometry is spherical and that individual clouds emit line radiation isotropically. These two assumptions will be relaxed in later sections.

The cloud properties and the continuum they are exposed to are the same as used in § 3 to calculate Figure 2. The range of the computed grid in Figure 2 is $7.0 \le \log n \le 14.0$ and $17.0 \le \log \Phi \le 24.0$, but integrations in $R_{\rm RW}$ are calculated on the subrange $7.0 \le \log n \le 14.0$ and $18.0 \le \log \Phi \le 22.25$. The lower flux limit corresponds to the radius of dust sublimation (Netzer & Laor 1993) where the presence of dust grains diminishes the line emission. The upper flux limit (or inner radius) of integration is set by the onset of line thermalization—dense clouds are primarily continuum emitters, the effect of the covering fraction function and the geometry. These boundaries are shown as dashed white lines in Figures 2*d*–2*i*. Note that the emission of C IV λ1549 (Fig. 2*d*), He II λ1640 (Fig. 2*e*), and He II λ4686 (Fig. 2*f*) decreases relative to the continuum outside these boundaries for the KG00 LOC model. For the assumed luminosity of NGC 5548 given by KG00, the upper flux limit of integration corresponds to a radius of $\sim$1 light day. In between the integration limits the contours of Figures 2*e* and 2*f* appear very similar. This suggests that it will be very difficult to create a significant difference between $R_{\rm RW}$(He II λ1640) and $R_{\rm RW}$(He II λ4686) for standard clouds.

5.1. *LOC Models*

The principal of the LOC model (Baldwin et al. 1995) is that clouds are distributed over a wide range in n and Φ, but those located at a density and flux that emit line radiation most effectively tend to dominate the integrated contribution to the observed line flux.

The differential covering fraction is written as the product of two functions, $\partial^2 C/\partial R \partial n \propto f(R)g(n)$. The functions $f(R)$ and $g(n)$ describe the physical structure of the BLR and in real situations are likely to be quite complicated. However, the emergent spectrum depends only weakly on the exact structure, so reasonable agreement with the observations is obtained using the simple power-law forms $f(R) \propto R^{\gamma}$ and $g(n) \propto n^{\delta}$. Thus,

$$\frac{\partial^2 C_f}{\partial R \partial n} \propto R^{\gamma} n^{\delta} . \quad (13)$$

Substituting $R \propto \Phi^{-1/2}$ into equation (13) and then equation (13) into equation (11) gives

$$R_{\rm RW} \propto \frac{\int_{\log \Phi_1}^{\log \Phi_2} \int_{\log n_1}^{\log n_2} (\partial F_l/\partial \Phi)\Phi^{-(\gamma+2)/2} n^{\delta+1} \, d\log n \, d\log \Phi}{\int_{\log \Phi_1}^{\log \Phi_2} \int_{\log n_1}^{\log n_2} (\partial F_l/\partial \Phi)\Phi^{-(\gamma+1)/2} n^{\delta+1} \, d\log n \, d\log \Phi} . \quad (14)$$

This equation determines the radius where there is significant emission. It has the advantage that it may be compared directly with observations.

How is it that this formula involving $\partial F/\partial \Phi$ is able to trace the spatial distribution of F? To illustrate the connection between the response-weighted approach and the intensity-weighted approach of the LOC model, consider the intensity-weighted radius $R_{\rm IW}$ defined by

$$R_{\rm IW} = \frac{\int_{\rm BLR} (jh) R \, dV}{\int_{\rm BLR} (jh) \, dV} . \quad (15)$$

For the isotropic LOC model, $R_{\rm IW}$ is given by

$$R_{\rm IW} \propto \frac{\int_{\log\Phi_1}^{\log\Phi_2}\int_{\log n_1}^{\log n_2} F\Phi^{-(\gamma+4)/2} n^{\delta+1}\, d\log n\, d\log\Phi}{\int_{\log\Phi_1}^{\log\Phi_2}\int_{\log n_1}^{\log n_2} F\Phi^{-(\gamma+3)/2} n^{\delta+1}\, d\log n\, d\log\Phi} . \quad (16)$$

Inspection of the integrands in the integrals in the denominators of equations (15) and (16) reveals that the weighting of $R_{\rm IW}$ is proportional to $F\Phi^{-(\gamma+3)/2}n^{\delta+1}$. This is the weighting used in the contour plots of Figures 2*d*–2*f* for C IV λ1549, He II λ1640, and He II λ4686, respectively (for the adopted LOC model of KG00 that has $\gamma = -1.2$ and $\delta = -1$). For comparison, Figures 2*g*–2*i* show the weighting of $R_{\rm RW}$ from equation (14) (also using $\gamma = -1.2$ and $\delta = -1$), which is proportional to $(\partial F/\partial\Phi)\Phi^{-(\gamma+1)/2}n^{\delta+1}$. The two sets of contour plots are nearly identical, showing that $F \propto (\partial F/\partial\Phi)\Phi$. This confirms that a significant portion of the emitting material responds in a linear way to modest (0.05 dex) changes of the continuum, which is a fundamental assumption of standard reverberation mapping theory (Blandford & McKee 1982). Thus, it is reasonable, at least for LOC models that use isotropically emitting clouds, that equation (14) is a good indicator of the relative location of line-emitting material.

LOC models are shown in the top six panels of Figure 4. The first row shows the intensity ratios I(C IV λ1549)/I(He II λ1640), I(He II λ1640)/I(He II λ4686), and I(C IV λ1549)/I(He II λ4686). Equation (4) is used for the calculations. The parameter space $[(-2.0 \le \delta \le 0.0) \times (-2.0 \le \gamma \le 0.0)]$ is considered. The location in parameter space of the LOC model used by KG00 is shown with a cross. The choice of parameters includes the range of the acceptable γ to be $-1.6 < \gamma < -0.5$, as found by KG00. In addition, earlier investigations by Baldwin (1997) suggest that $\delta \approx -1$. We do not consider values significantly outside this range because they give poor fits to the observed reverberation times and intensities of other bright emission lines not studied here.

The intensity ratio contours may be compared with the observed line flux ratios from Table 1. The C IV λ1549/He II λ1640 ratios determined from the 1989 and 1993 observing campaigns overlap with each other and also with the value calculated using the KG00 model. The (very wide) error bars on the C IV λ1549/He II λ4686 measurement from the 1989 campaign also include the KG00 value.

We do not vary the form of the ionizing continuum. The ratio of C IV λ1549 to recombination lines depends on the continuum shape since this is the ratio of a strong coolant to the recombination rate, which is basically the Stoy ratio (Osterbrock 1989). We could have adjusted the continuum shape to reproduce the C IV/He II intensity ratios but do not do so here. The second row of the top panels of Figure 4 shows the ratios $R_{\rm RW}$(C IV λ1549)/$R_{\rm RW}$(He II λ1640), $R_{\rm RW}$(He II λ1640)/$R_{\rm RW}$(He II λ4686), and $R_{\rm RW}$(C IV λ1549)/$R_{\rm RW}$(He II λ4686) for the LOC model. Equation (14) is used to calculate the $R_{\rm RW}$ up to a multiplicative constant.

The observed lag ratios in Tables 2 and 3 are contaminated by O III] λ1663 mixed in with the He II λ1640 line. To estimate the correction to the measured lag, we must first estimate the contribution of O III] to the total intensity. The observed O III] λ1663/He II λ1640 intensity ratio is about 0.5, while the LOC model with the KG00 parameters ($\gamma = -1.2$, $\delta = -1$) predicts 0.7. Figure 5 shows the expected correction to $R_{\rm RW}$(He II λ1640) as a function of I(He II λ1640)/I(He II λ1640+contaminating O III] λ1663), for both the LOC model and the pressure-law model (labeled Gauss) described below. The ratio I(He II λ1640)/I(He II λ1640+contaminating O III] λ1663) was found by summing the distributions of O III] λ1663 and He II λ1640 emissivities on the $\log n$–$\log\Phi$ plane as predicted by the model, but scaling O III] λ1663 by a factor that varied from 0 to 1.0. $R_{\rm RW}$ for the resulting He II–O III] blend was then calculated and compared to $R_{\rm RW}$ for the He II line alone to produce the correction.

Figure 5 shows that O III] contamination should lead to only a $\sim$10% effect (a decrease) in the *observed* He II λ1640 lag time. The effect is small because, although O III] emits most strongly from a radius about 2 times farther out than the peak of the He II emissivity, the He II emission is spread out over a broad range extending out to rather large radii.

The model ratios may now be compared to the observed lag ratios in Tables 2 and 3. Because of the large observed errors on the lag ratios, definitive claims cannot be made about whether or not LOC models are consistent or inconsistent with observations. The results, however, are suggestive. Note that whether or not we allow for a small correction for O III], the observed lag ratio lag(C IV λ1549)/lag(He II λ1640) $\sim$ 3.0 (see Tables 2 and 3) is not achieved anywhere by the LOC model in the parameter space considered nor is the observed lag ratio lag(He II λ1640)/lag(He II λ4686) $\sim$ 0.4. The predicted values are 2.4 and 0.8 σ away from these observed values. On the other hand the observed lag ratio lag(C IV λ1549)/lag(He II λ4686) $\sim$ 1.1 is achieved by the LOC model in the parameter space considered. This suggests that there is a problem with the He II λ1640 line rather than the He II λ4686 line. The model predicts a response of He II λ1640 roughly contemporaneous with He II λ4686 and C IV λ1549. The observations indicate an earlier response, by a factor of about 3.

5.2. *Radius-dependent Pressure-Law Models*

In order to see if the discrepancies with the observations might be just an artifact of the LOC model, we now consider a quite different class of models that are radius-dependent pressure laws (Goad et al. 1993). Here

$$n = 10^{10}\left(\frac{\Phi}{10^{18.5}}\right)^{m}, \quad (17)$$

where equation (17) defines a straight line in the $\log n$–$\log\Phi$ plane. For reference, $m = 0$ defines a vertical line (constant density). The line is constructed to pass through the point $\log n = 10.0$ and $\log\Phi = 18.5$ to be in accord with the conditions of "standard" BLR cloud conditions (Davidson & Netzer 1979). The ionization parameter along this line is $U = \Phi/nc \approx 10^{-2}(\Phi/10^{18.5})^{1-m}$. Observations indicate that the BLRs of AGNs are ionization stratified with lower ionization lines dominating at greater radii (Peterson 1993). Thus, if radius-dependent pressure-law models apply to the BLR, then U must decrease with increasing radius so that $m \le 1$. In addition denser BLR clouds may lie at smaller radii (and therefore higher Φ; Brotherton et al. 1994). We therefore restrict m to $0 \le m \le 1$. As with the LOC model, a differential covering factor in the form of a

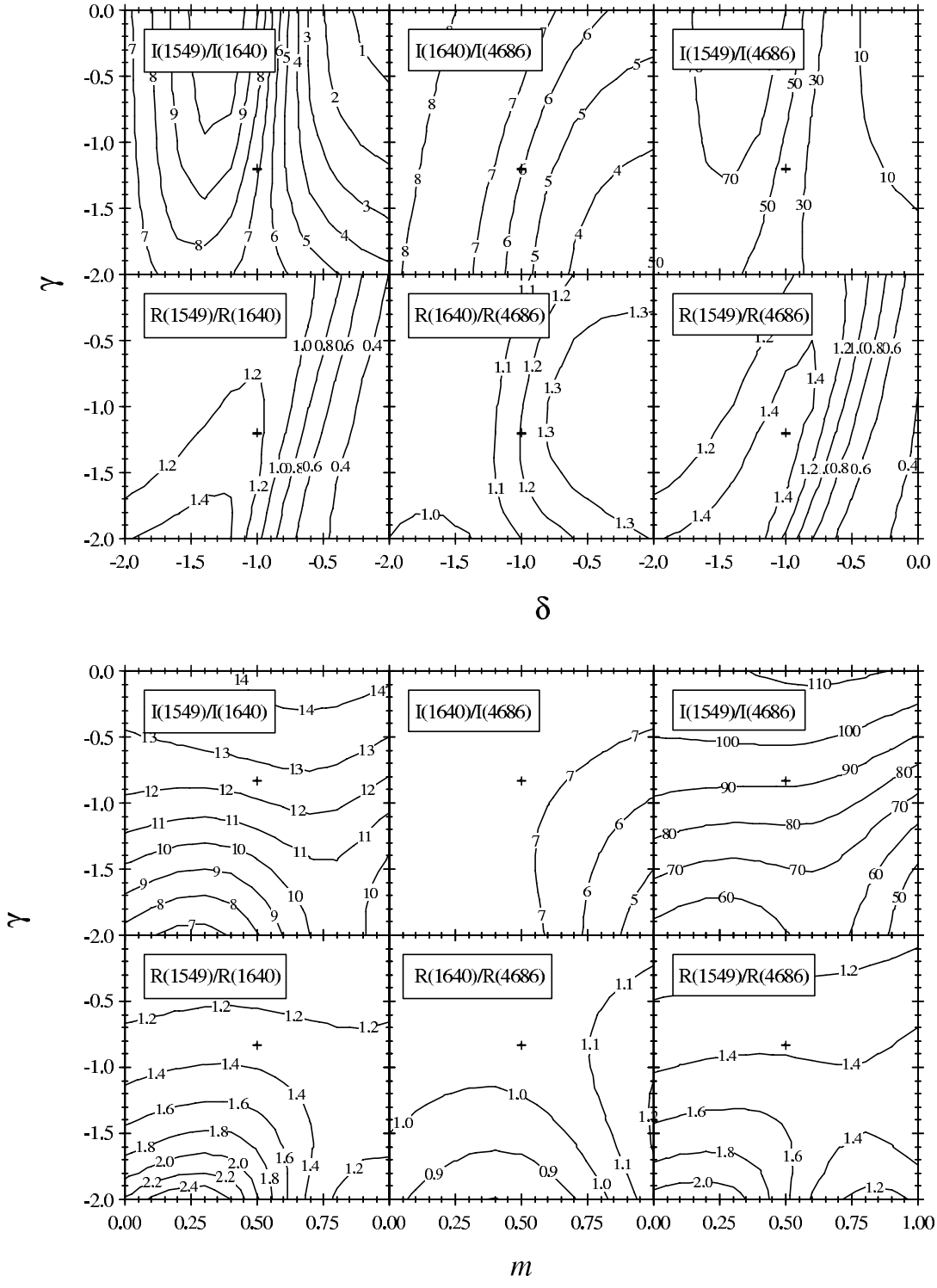

FIG. 4.—*Top*: I(C IV λ1549)/I(He II λ1640), I(He II λ1640)/I(He II λ4686), and I(C IV λ1549)/I(He II λ4686) (*first row*) and $R_{\rm RW}$(C IV λ1549)/$R_{\rm RW}$(He II λ1640), $R_{\rm RW}$(He II λ4686)/$R_{\rm RW}$(He II λ1640), and $R_{\rm RW}$(C IV λ1549)/$R_{\rm RW}$(He II λ4686) (*second row*) for LOC models as functions of the differential covering factor parameters γ and δ. A cross at $\gamma = -1.2$, $\delta = -1.0$ marks the parameters of the optimal LOC solution from KG00. *Bottom*: Same as top panel except that pressure-law models are shown as functions of m and γ. A cross marks the solution $m = \frac{1}{2}$ and $\gamma = -\frac{5}{6}$ from Goad et al. (1993).

power law in radius is assigned, thus,

$$\frac{\partial C_f}{\partial R} \propto R^{\gamma} \, . \tag{18}$$

We normalized the models in the same way as Goad et al. (1993), but unlike them we used a constant column density for simplicity. To facilitate integration on the coarse computed grid, we assign a differential cover factor in the form of a Gaussian distribution in $\log n$ with standard deviation 1.0 centered on equation (17). Thus, while not an exact radius-dependent pressure-law model (due to the Gaussian width), this distribution is 5 orders

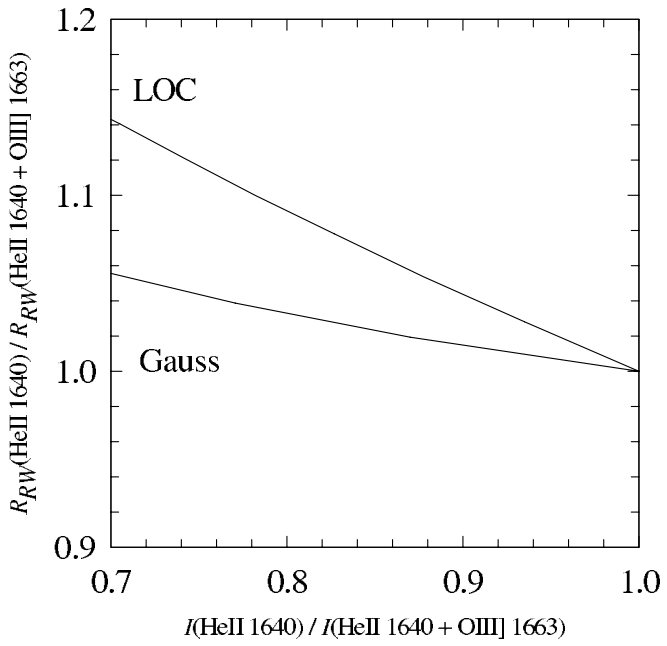

FIG. 5.—Plot showing the correction to be applied to the observed reverberation of He II λ1640 when it is contaminated with O III] λ1663 as a function of the fraction of the intensity of He II λ1640 contaminated with O III] λ1663. We caution that in this figure all of the He II λ1640 intensity is included in the blend, while only part of the O III] λ1663 is included. The plot therefore shows the effect on reverberation corresponding to varying degrees of O III] λ1663 contamination of He II λ1640. See the text for details.

of magnitude more restricted in density than the LOC models of § 5.2.

The first row of the bottom six panels of Figure 4 shows the intensity ratios C IV λ1549/He II λ1640, He II λ1640/He II λ4686, and C IV λ1549/He II λ4686 for the pressure-law model. The parameter space $(0.0 \le m \le 1.0) \times (-2.0 \le \gamma \le 0.0)$ is considered. A cross at $m = \frac{1}{2}$ and $\gamma = -\frac{5}{6}$ marks the parameters of an idealized $n \propto R^{-1}$ pressure-law model from Goad et al. (1993) that predicts reasonably well the reverberation response of the bright emission lines of NGC 5548.

As with the LOC model, the intensity ratio contours of the pressure-law model may be compared with the observed line ratios C IV λ1549/He II λ1640, He II λ1640/He II λ4686, and C IV λ1549/He II λ4686 from Table 1. The predicted ratios of the pressure-law model fair less well than those of the LOC model. For example, when the range of the observed flux ratio C IV λ1549/He II λ1640 from either the 1989 or the 1993 observing campaigns of NGC 5548 is mapped onto the corresponding intensity ratio contours, the idealized pressure-law model ($m = \frac{1}{2}$ and $\gamma = -\frac{5}{6}$) is not included.

The predicted O III]/He II ratio is 1.5. Other choices of the model parameters could lower this predicted value by including a different part of the $\log n - \log \Phi$ plane but are unlikely to satisfy the many other conditions set by the reverberation results and the strengths of the other emission lines. An alternate possibility is that the abundances of the α-elements are lower, by about a factor of 2, than were used in our models. Figure 5 shows the expected correction to the He II lag time for the pressure-law model, calculated in the same way as for the LOC model. Again, the correction to $R_{\rm RW}$ is only about 10% and therefore will be ignored here.

The second row of the bottom panels of Figure 4 shows the ratios $R_{\rm RW}$(C IV λ1549)/$R_{\rm RW}$ (He II λ1640), $R_{\rm RW}$(He II λ1640)/$R_{\rm RW}$(He II λ4686), and $R_{\rm RW}$(C IV λ1549)/$R_{\rm RW}$(He II λ4686) for the pressure-law model. The model ratios are compared to the corresponding lag ratios in Tables 2 and 3. Note that the observed lag ratio lag(C IV λ1549)/lag(He II λ1640) $\sim$ 3.0 is not achieved anywhere by the pressure-law model in the parameter space considered nor is the observed lag ratio lag(C IV λ1640)/lag(He II λ4686) $\sim$ 0.4 or the observed lag ratio lag(C IV λ1549)/lag(He II λ4686) $\sim$ 1.1. Thus, the pressure-law model has problems with all three response ratios considered here. The pressure-law model F of Goad et al. (1993) is one of constant density and column density, and so its cloud distribution cuts across the largest number of contours in Figures 2*d*–2*i* (a vertical line in these plots). It also has the property of having a steeply falling covering fraction distribution with radius ($\gamma = -9/6$). Together these conspire to widely separate the emission-line lags. However, Table 4 in Goad et al. (1993) and the bottom left-hand panel of our Figure 4 indicate that even this model produces a lag ratio lag(C IV λ1549)/lag(He II λ1640) < 1.8, far short of the observed value of $\sim$3.

The scatter and error bars in the observed reverberation lag ratios are far too large to make definitive claims about which model is best. For example, based on the above analysis, one cannot conclude that the LOC model is any better or worse than the pressure-law model at predicting the intensity or lag ratios considered in this paper. Rather, the important point of these two sections is that a wide range of models consisting of clouds distributed in density and radius and unique in density with radius is unable to account for *both* the observed short reverberation time of He II λ1640 relative to C IV λ1549 and possibly He II λ4686.

5.3. *Effect of Internal Cloud Parameters*

We have focused on this pair of He II lines because of their simplicity. Resonance lines of He II occur at energies that can ionize both hydrogen and helium. Either this destruction or conversion by the Bowen mechanism (Osterbrock 1989) acts to prevent large optical depths from building up in He II subordinate lines. As a result the optical and UV lines are formed mainly by recombination, and the emission spectrum is mainly determined by the branching ratios from upper levels. There is only a weak (<20% typically) density and temperature dependence due to details of the atomic physics. In particular the He II recombination spectrum has no direct dependence on the continuum shape or gas composition. The spectrum will be near "case B" and have no dependence on the column density as long as the column density is large enough to allow the He II Lyman lines to be optically thick. Ferland (1999) discusses the smaller column density case and shows that the spectrum goes over to the moderately different "case C" but that such optically thin clouds are very inefficient radiators and would be nearly invisible. It is hard to imagine realistic conditions where the He II emission would be far from its simplest expectations.

We conclude this section with brief comments on four additional factors that, at first sight, might influence the observed lag times: (1) BLR cloud size, (2) recombination times, (3) negative responsivity clouds, and (4) nonlinear response. For each of these, we find that the impact on I and $R_{\rm RW}$ is negligible for the types of models considered here

and therefore are probably not important in any realistic BLR model.

5.3.1. *Cloud Size*

The flux ordinate on the $\log n - \log \Phi$ plane may be converted into a distance scale if a luminosity is assumed. The luminosity of NGC 5548 given by KG00 gives an inner radius of integration of $\sim$1 light day. Spherical clouds with column density $\sim 10^{23}$ cm^{-2} with $\log n \leq 8.0$ will completely fill the volume at this radius and cover the continuum source. In general clouds in the upper left-hand corner of the $\log n - \log \Phi$ plane will have problems fitting in the BLR at the given normalization of flux with radius. Clouds in this region must therefore be excluded from integrations over the region. In any case clouds in this region are fully ionized and contribute little to the integrated line emission or the reverberation response (for all of the same reasons, KG00 excluded these clouds from consideration).

5.3.2. *Recombination Time*

The recombination time is roughly proportional to $(nT)^{-1}$. The recombination time is always shorter than the variability time except when the gas is heated to the Compton temperature, but this gas does not contribute to the net emission. The jagged white line superposed on the contour plots of Figures 2*d*–2*i* (and the jagged solid line superposed in Fig. 3) corresponds to a recombination time of $\sim$1 day. To the right of this line recombination times are shorter. In the region of significant emission the recombination time is only a few minutes. Recombination time delay effects therefore need not be considered in reverberation calculations.

5.3.3. *Negative Cloud Responsivity*

Figures 2*a*–2*c* all have regions where $\partial F/\partial \Phi < 0$. The region is roughly above a diagonal running from the lower left-hand corner to the upper right-hand corner of each figure. Clouds in this region have line emissivities that *decrease* with an increase in Φ. If this also implies that $\eta < 0$ (provided that the function f and or $\partial^2 C/\partial n \partial R$ does not somehow compensate), then the clouds are said to have "negative responsivity." Figures 2*d*–2*i* show that the LOC weighting strongly suppresses the contribution to both the emission and emission response of negative responsivity gas. Even if there was a distribution of column densities, it would mainly affect the low-ionization lines because the high-ionization lines form near the inner edge of the cloud. The region in the $\log n - \log \Phi$ plane where $\partial F/\partial \Phi < 0$ (the triangular region of the upper left-hand half of Figs. 2*g*–2*i*) has very nearly a zero value. Thus, the LOC models we computed have little net emission from negative responsivity clouds, and the overall effect is that the lines investigated here respond positively. The pressure-law models we calculated also do not include any significant contribution from negative responsivity gas.

5.3.4. *Nonlinear Emission-Line Response*

The goal of reverberation analysis is to reconstruct the spatial distribution of line emission or, at the very least, the values of lower order moments such as $R_{\rm RW}$. Formulae for $R_{\rm RW}$ (eq. [5]) assume that line emissivity either has a strict linear response to changes in Φ (Blandford & McKee 1982) or that changes in Φ are sufficiently small so that the emissivity is well represented by linearization. Locations on the $\log n - \log \Phi$ plane where problems may arise if either of the above assumptions are not valid are on the ridge lines of emission where the concavity of emission with increasing Φ is largest. These ridge lines are seen as sharp bends in the contour lines of Figures 2*a*–2*c* and (as mentioned earlier) are where the gas begins to transition to its coronal phase. We note that when weighted by the representative models discussed in this paper, emission from the regions near the ridge lines are suppressed and have little effect on $R_{\rm RW}$. Figures 2*d*–2*i* illustrate that this is the case for the best-fit model of KG00, where near the locations of the respective ridge lines, weighted emission is only $\sim$10% of the maximum and the weighted maximum emission occurs far from the ridges.

Given the above comments, we assume that the response is *locally* linear. Note that this does not mean a 1 : 1 response of the whole line to the continuum. Rather, if the continuum is perturbed, a new line flux distribution results locally at *every* point in the $\log n - \log \Phi$ plane with equation (8) determining the local η (responsivity). Calculations assuming a perturbed light curve or using a full nonlinear treatment show that, for the case of NGC 5548, there is little difference in the calculated responsivity-weighted radii. Compare, for example, the results of O'Brien, Goad, & Gondhalekar (1994) with O'Brien, Goad, & Gondhalekar (1995). In the latter case, the locally linear approximation was not used, and instead a full nonlinear treatment was applied to investigate how large changes in luminosity affect the calculation of the responsivity-weighted radius. The anisotropic responsivity-weighted radii, for their model F, for these two cases are as follows: For He II λ1640, the responsivity-weighted radius is 4.5 light days using the locally linear approximation and a static BLR with a small continuum perturbation versus 3.9–5.0 light days (4.4 light day mean) using the λ1350 continuum from the 1989 campaign to drive the BLR model. For C IV λ1549, the responsivity-weighted radius is 6.1 light days using the locally linear approximation for a static BLR with small perturb versus 3.5–7.7 light days (5.8 light day mean) using the λ1350 continuum from the 1989 campaign to drive the BLR model. O'Brien et al. (1995) altered their model F so that it would have fully ionized gas within 10 light days of the source (so that a large contingent of the gas was optically thin in the mean state). The full nonlinear treatment in the line response was 10.6–16.2 light days for He II λ1640 and 15.0–19.6 light days for C IV λ1549. The important conclusions from these calculations are that (1) there is no significant *relative* difference between He II λ1640 and C IV λ1549 in the perturbed or nonlinear calculations and (2) lag ratios as large as $\sim$3 are not achieved.

The weighting of the models investigated in this paper scales as a power law. As a result a change in the ionizing flux may be interpreted as equivalent to a vertical shift of the $\log \Phi$ limits of integration (the dotted lines in Figs. 2*d*–2*i*). Along the upper boundary the weighted contribution decreases with an increase in $\log \Phi$, whereas along the lower limit the weighted contribution increases. The two effects roughly offset one another as long as neither of the limits approaches the weighted emission peaks. Numerical experiments on the best-fit model of KG00, in which the flux limits are changed by a factor of $\sim$5 (a vertical shift of $\sim$0.7 dex in the $\log n$–$\log \Phi$ plane), have little effect on the relative reverberation response of the C IV λ1549, He II λ1640, and He II λ4686 lines. We conclude that even large changes in Φ (a factor of $\sim$5)

will have little effect on the relative responses of the lines investigated here.

6. BEAMING AND DISK OBSCURATION

The common assumption of all the models of §§ 5.2 and 5.3 is that emission from clouds is both isotropic and unobscured. Here we investigate whether or not beaming, possibly coupled with obscuration by a disk, can reduce the model ratio $R_{\rm RW}$(He II λ1640)/$R_{\rm RW}$(He II λ4686) and increase the model ratio $R_{\rm RW}$(C IV λ1549)/$R_{\rm RW}$(He II λ1640) so that the corresponding observed lag ratios are more consistent with the best-fit models (e.g., the models corresponding to the crosses in Fig. 4). For beaming, we take the extreme (but computationally tractable) case of "pancake" clouds with the normal of the continuum-facing surface pointing directly at the continuum engine. Simulations predict the fraction of the emission, directed toward the source of ionizing radiation. The portion of the emission from the cloud beamed toward the observer (defined in § 2 as h) is then given by

$$h \propto \begin{cases} h_D\mu\,, & \text{for } 0 \le \mu \le 1\,, \\ -h_I\mu\,, & \text{for } -1 \le \mu < 0\,, \end{cases} \tag{19}$$

where h_D is the fraction of the total emission beamed out the back (or dark) side of the cloud, h_I is the fraction of the total emission beamed out the front (or illuminated) side of the cloud (so that $1 - h_D = h_I$), and $\mu = \cos\theta$, where θ is the angle between a ray from the continuum source to the observer and a ray from the continuum source to a cloud. For simplicity, we assume that all functions of angle are independent of R. Introducing equation (19) into equation (5) gives

$$R_{\rm RW} = \frac{\int_\Omega h(1+\mu)\,d\Omega \int_{R_1}^{R_2} (\partial j/\partial\Phi) R\,dR}{\int_\Omega h\,d\Omega \int_{R_1}^{R_2} (\partial j/\partial\Phi)\,dR}\,, \tag{20}$$

where we have used the fact that $L_c = 4\pi R^2\Phi$ may be factored out of the integrals.

We now hypothesize that an obscuring disk blocks our view of the far side of the BLR. The disk is oriented at polar angle Θ with respect to the direction to the observer (the Z-axis). The integration in angle therefore is not over a full 4π sr but over a smaller unblocked solid-angle region that we symbolize by Ω. Part of the solid angle includes the region where the observer views the dark side of the cloud. In the remaining region an observer sees the illuminated side of the cloud. Separating the radial and angular parts of equation (20) gives

$$R_{\rm RW} = G(\Omega) R_{\rm RW,\,isotropic}\,, \tag{21}$$

where

$$G(\Omega) = \frac{\int_\Omega h(1+\mu) d\Omega}{\int_\Omega h\,d\Omega} \tag{22}$$

and $R_{\rm RW,\,isotropic}$ is $R_{\rm RW}$ as given by equation (9) but with the subscript "isotropic" is added to remind us that it is the isotropic case. The function $G(\Omega)$ multiplying $R_{\rm RW,\,isotropic}$ is therefore the factor by which the isotropic case is modified to give the anisotropic case (for this simplified scenario).

We now integrate equation (22). To simplify visualization, we consider a unit spherical shell section of the BLR

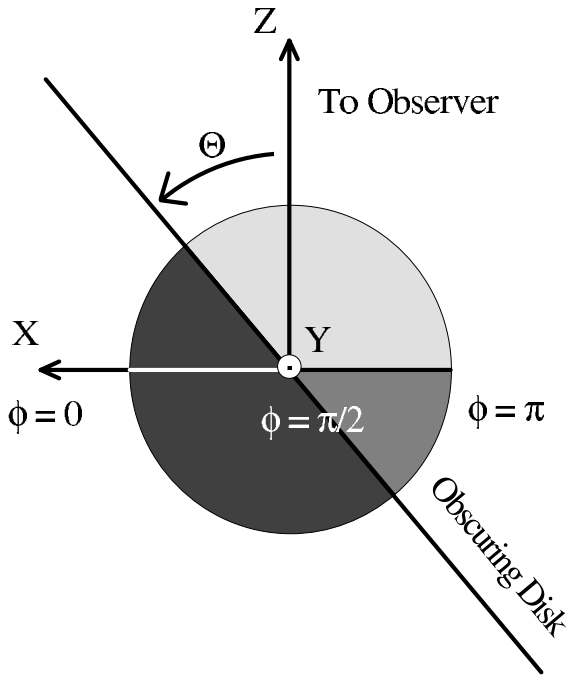

FIG. 6.—Schematic showing the regions of integration for the calculation of $G(\Omega)$. An obscuring disk is viewed edge on. It cuts through the computational sphere at an angle Θ with respect to the observer direction (the Z-axis). Clouds below this disk are hidden from the observer. The X-axis (corresponding to $\phi = 0$) is to the left, and the Y-axis (corresponding to $\phi = \pi/2$) is out of the plane of the page. The observer views the dark side of the clouds if they lie above the X-Y plane and the illuminated sides of the clouds if they are unobscured and lie below the X-Y plane.

(see Fig. 6). Observers see emission from clouds with $Z > 0$ originating from the dark side of the cloud. Observers see emission from clouds with $Z \le 0$ originating from the illuminated side of the cloud. Any emission originating from below the bisecting plane does not reach the observer. A contour plot of $G(\Omega)$ as a function of Θ in degrees from 0° to 90° and h_D from 0 to 1 is shown in Figure 7. The surface cut by $\Theta = 0°$ is equivalent to no obscuration. Note that at $\Theta = 0°$, $h_D = 0.5$, we have $G(\Omega) = 1$, as we should have for isotropy and no obscuration. Values of $G(\Omega)$ for isotropic emission with an obscuring disk lie on the horizontal line $h_D = 0.5$. The general trend is that increasing h_D or Θ results in decreasing $G(\Omega)$.

The CLOUDY computations h_D for the lines C IV λ1549, He II λ1640, and He II λ4684 are shown in Figures 2*j*–2*l*. Lighter regions shows where h_D exceeds the 0.5 contour threshold by a few percent. Successive contours and darker regions correspond to a 0.1 decreases of h_D. Over the regions where there is significant emission from C IV λ1549, He II λ1640, and He II λ4686 most clouds with column densities $\ge 10^{23}$ cm^{-2} have $h_D \le 0.5$. To illustrate, the emission-weighted average of h_D for C IV λ1549, He II λ1640, and He II λ4686 is 0.26, 0.33, and 0.41, respectively. These three values are shown as horizontal dashed lines in Figure 7. Overall, the C IV λ1549 line is the most anisotropic (smallest h_D) followed by the He II λ1640 line and then He II λ4686. To estimate the magnitude of the correction on ratios of $R_{\rm RW}$, the ratios of $G(\Omega)$ as a function of Θ are found along lines of emission-weighted h_D. Based on this the maximum correction to $R_{\rm RW}$(C IV λ1549)/$R_{\rm RW}$(He II λ1640) is $\sim$1.2 at a disk orientation $\Theta \approx 40\overset{\circ}{.}5$, the maximum correction to

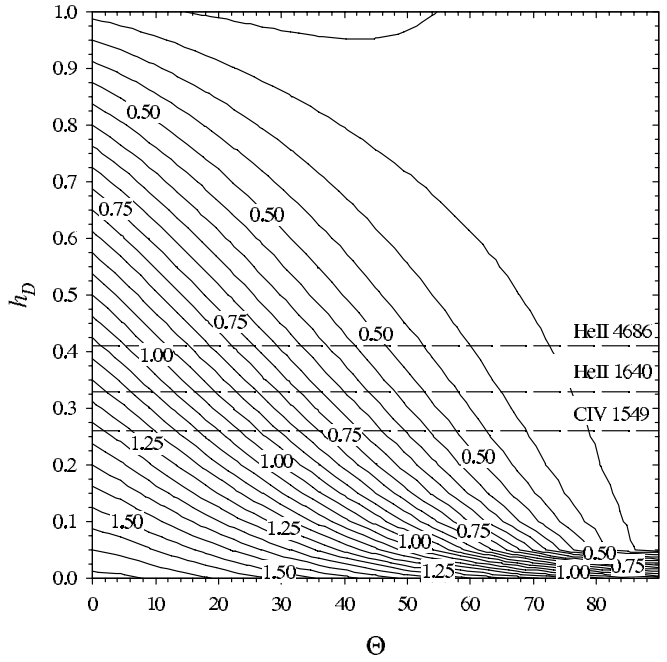

FIG. 7.—Contour plot of $G(\Omega)$ as a function of f_D and Θ. The horizontal lines show the emissivity-weighted average of f_D for C IV λ1549, He II λ1640, and He II λ4686.

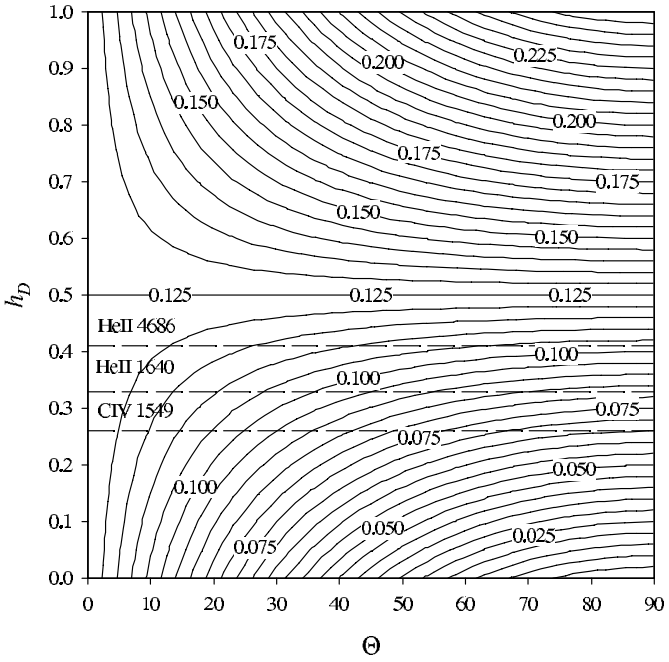

FIG. 8.—Contour plot of $G(\Omega)$ for intensity. The horizontal lines show the emissivity-weighted average of f_D for C IV λ1549, He II λ1640, and He II λ4686.

R_{RW}(He II λ1640)/R_{RW}(He II λ4686) is ∼1.1 at a disk orientation Θ ≈ 31°.5, and the maximum correction to R_{RW}(C IV λ1549)/R_{RW}(He II λ4686) is ∼1.3 at a disk orientation Θ ≈ 36°.0. If we apply these corrections to the optimal LOC model (marked by the cross in Fig. 4), we see that R_{RW}(C IV λ1549)/R_{RW}(He II λ1640) is boosted from ∼1.2 to ∼ 1.2 × 1.2 ≈ 1.4, R_{RW}(He II λ1640)/R_{RW}(He II λ4686) is boosted from ∼1.1 to ∼ 1.1 × 1.1 ≈ 1.2, and R_{RW}(C IV λ1549)/R_{RW}(He II λ4686) is boosted from ∼1.4 to ∼ 1.4 × 1.3 ≈ 1.8. These corrections move R_{RW}(C IV λ1549)/R_{RW}(He II λ1640) slightly closer to the observed value of ∼3 (Tables 2 and 3) but move R_{RW}(He II λ1640)/R_{RW}(He II λ4686) and R_{RW}(C IV λ1549)/R_{RW}(He II λ4686) away from their observed values of ∼0.4 and ∼1.1, respectively. There are similar results for the pressure-law models. We conclude from this analysis that it is not possible to simultaneously satisfy the observed response ratios with *any* of the broad range of model types considered here.

A similar analysis was done to estimate the effect of anisotropic emission on line intensity ratios. A contour plot of $G(\Omega)$ for intensity is shown in Figure 8 as a function of Θ and h_D. The horizontal dashed lines show the same emission-weighted h_D as in Figure 7 for C IV λ1549, He II λ1640, and He II λ4686. Relative differences in $G(\Omega)$ from one h_D value to another, for obscuring disk angle Θ, give the correction to the intensity ratios for the case of isotropic beaming. We note that $h_D = 0.5$ means symmetry of front versus back surface emission. Because the clouds are pancake shaped, however, beaming is still present. In addition there is still obscuration by a disk. This is why $G(\Omega)$ does not equal 1 when $\Theta = 0^\circ$ and when $h_D = 0.5$.

Ratios of $G(\Omega)$ using the emission-weighted h_D of I(C IV λ1549/I(He II λ1640), I(He II λ1640)/I(He II λ4686), and I(C IV λ1549)/I(He II λ4686) intensity ratios were calculated. The ratios all decrease, from a value of 1 at $\Theta = 0^\circ$, with increasing Θ to the maximal possible decrease at $\Theta = 90^\circ$ for which the correction to I(C IV λ1549)/I(He II λ1640), I(He II λ1640)/I(He II λ4686), and I(C IV λ1549)/I(He II λ4686) is 0.71, 0.88, and 0.63, respectively. If we apply these values to the optimal LOC model (marked by crosses in Fig. 4), we see that I(C IV λ1549)/I(He II λ1640) is reduced from ∼9.0 to ∼ 9.0 × 0.71 ≈ 6.4 (vs. 9.7 ± 2.1 using the tighter result from the 1993 campaign; Table 1), I(He II λ1640)/I(He II λ4686) is reduced from ∼7.0 to ∼ 7.0× 0.88 ≈ 6.2 (vs. 5.1 ± 3.0; Table 1), and I(C IV λ1549)/I(He II λ4686) is reduced from ∼70 to ∼ 70 × 0.63 ≈ 44 (vs. 48 in Table 1). Thus, these corrections move I(C IV λ1549)/I(He II λ1640) slightly out of the observed range, but since the I(C IV λ1549)/I(He II λ1640) intensity ratio is sensitive to the shape of the ionizing continuum, this discrepancy is not necessarily an issue. The ratios I(He II λ1640)/I(He II λ4686) and I(C IV λ1549)/I(He II λ4686) are reduced to agree with the (albeit very uncertain) observations. Thus, while the intensity ratios are reasonably well predicted, the reverberation responses are not.

7. CONCLUSIONS

We know directly from the reverberation measurements that the BLR gas is distributed over a wide range in radial distance from the ionizing continuum source. In the preceding sections we have considered a variety of distributed BLR models, including ones with anisotropic line emission, and shown that in all cases the differences in lag times between the He II λ1640 and C IV λ1549 line are predicted to be much smaller than the observed differences and that contrary to the limited observations comparing He II λ1640 and He II λ4686, these two lines are expected to vary almost simultaneously. Table 4 summarizes both the model results and the observations.

While there may be some other type of model that would resolve this conflict with the observations, we do not know what it is. The LOC and pressure-law models we have discussed here span the range of BLR models being considered

TABLE 4
SUMMARY OF MODEL RESULTS AND OBSERVATIONS

	Intensity Ratio			Lag Ratio		
Model	C IV λ1549/He II λ1640	1640/4686	C IV/4686	C IV/1640	1640/4686	C IV/4686
Optimized LOC ($\gamma = -1.2, \delta = -1.0$).....	9	7	70	1.2	1.1	1.4
Pressure law ($m = 1/2, \gamma = -5/6$)	13	7	90	1.3	1.05	1.4
LOC beamed+obscuring disk[a].....	6	6	44	1.4	1.2	1.8
Observed (NGC 5548).....	10	5	48	3.3	0.4	1.1

[a] The maximal correction, based on the emission-weighted h_D, applied to the optimized LOC model.

today since most dynamic or kinematic models invoke distributions of clouds at a given radius or clouds of a specific type at each radius.

Although the effect of any single parameter studied here is much too small to cause the observed lag ratios, it is always possible that a number of them have conspired together to produce the observed result. If so, these would have to be general properties of AGNs since discrepant He II λ1640 lag times are seen in many objects (Table 3).

On the observational side, C IV λ1549/He II λ1640 lag ratios are a factor of 2–3 larger than the model predictions measured in six campaigns covering five different AGNs, strongly suggesting that this is a real effect despite the substantial uncertainty in each set of observations. The small He II λ1640/He II λ4686 lag ratio is based on only one campaign and so is therefore somewhat uncertain, and in addition, He II λ4686 is blended with Fe II (Fig. 1). Maoz et al. (1993) found that in NGC 5548 the small UV bump due to Fe II (λλ2260–2655) varies with a lag time of ∼10 days during the 1989 campaign, essentially the same as the reported He II λ4686 and C IV lag times. If the optical Fe II lines vary on the same timescale as the UV ones (which is unknown and not necessarily expected), it may be that the He II λ4686 lag measurement is spurious and that both He II lines vary on the same (unexpectedly rapid) timescale. However, the He II spectrum is very simple, and the He II λ4686/C IV λ1549 lag ratio is close to the expected value, suggesting again that the 1640 lag is unexpectedly short.

The thrust of this paper has been on He II and the problems models have in predicting the overly rapid response of the He II λ1640 line. By contrast, models *do* predict the high-ionization fast-responding line N V λ1240 in NGC 5548. To illustrate, the observations yield a C IV λ1549/N V λ1240 lag ratio of ∼2.4 and ∼2.8 for the 1989 and 1993 campaigns, respectively, of NGC 5548 (with perhaps a 50% error on the lag of the N V λ1240 line), and the KG00 optimal model gives a lag ratio of C IV λ1549/N V λ1240 ∼ 2.0. This agreement suggests that our results are robust to the details of the high-flux, inner region of the BLR where both the He II lines *and* N V λ1240 peak in emission. This strengthens the argument that it is the He II λ1640 line that is a problem.

The most straightforward explanation is that we are measuring some other feature blended with He II λ1640. What could this extra feature be?

In principle the He II λ1640 line could be dominated by an extra, rapidly varying component that does not produce much He II λ4686 or C IV λ1549. Comparison of Figures 2*a* and 2*b* shows that gas with $\log n \sim 12$–13, $\log \Phi \sim 24$ could produce λ1640 but little λ1549, but Figures 2*b*, 2*c*, and 3 together show that there is no location on the $\log n$–$\log \Phi$ plane where large amounts of λ1640 can be produced without also producing lots of λ4686 emission. Even if there were such a situation, then the mean λ1640/λ4686 intensity ratio should be very large, which does not appear to be the case (albeit with very large observational uncertainties, as is discussed in the Appendix).

We suggest that a more likely candidate is a variable *absorption* feature from the continuum source itself. The ultraviolet continuum source is usually assumed to be dense thermal matter, probably the skin on an accretion disk. Current disk models do not accurately predict the continuum spectrum at the level of detail that would include absorption lines; in fact, there is a well-known problem in that hydrogen Lyman continuum absorption is predicted but not seen (Antonucci et al. 1996; Antonucci, Kinney, & Ford 1989). We postulate that an absorption feature due to He II λ1640 or some other nearby line is produced in the skin of the accretion disk and responds immediately to changes in the continuum level coming from the disk. The response of this component would then be mixed with the slower response of He II emission produced in the BLR to give the observed result. To produce the observed effect, such an absorption feature would have to diminish in equivalent width as the continuum level increased since the net feature at λ1640 is always observed to have a strong positive response to continuum variations. An obvious difficulty with this interpretation is that no other atmospheric absorption features are known.

The above is at present just speculation. What we actually have found here is that a wide range of models of the BLR indicate that He II λ1640, He II λ4686, and C IV λ1549 should all have very similar reverberation lag times. The available observations appear to contradict this, but the uncertainties are large. An obvious next step that we are currently initiating is to reexamine the extensive existing data from AGN reverberation monitoring campaigns in order to better test whether or not He II λ1640 really does have a several times shorter lag time than C IV and whether or not the He II λ1640/λ4686 intensity ratio is consistent with the expected range of 6–8.

If the contradiction between the models and observations persists and is significant, we will then need to more carefully consider what revisions are required in our picture of the BLR.

This work was supported by the NSF and NASA through grants AST 00-71180 and NAG 5-8212. We thank the anonymous referee for stimulating and helpful comments.

APPENDIX

THE He II λ1640/4686 INTENSITY RATIO IN NGC 5548

We discuss here the various corrections that we believe need to be applied to the published λ1640 and λ4686 line strengths from C91 and D93 before they can be used to derive the He II λ1640/He II λ4686 intensity ratio. To start with, a 3.5% correction of the λ1640/λ4686 ratio is needed because the fluxes quoted in D93 are in rest frame, but more important are the contributions of the contaminants to each line, the uncertainties associated with the absolute flux calibration of the optical spectra, the possibility of nonlinear response of the *IUE* detectors at low light levels (Koratkar et al. 1997), and the possibility of reddening within NGC 5548.

C91 reported a mean flux of the He II λ1640/O III] λ1663 blend of 77.8 in units of 10^{-14} ergs cm^{-2} s^{-1} (observed frame) for the 1989 *IUE* monitoring campaign of NGC 5548. Using the *HST* Faint Object Spectrograph (FOS) spectrum of NGC 5548 during a very low state in the continuum and broad emission lines, Goad & Koratkar (1998) measured a narrow-line flux in He II λ1640 of only 6.0, leaving 71.8 to originate in the BLR. This measurement is consistent with the unreported measurement of narrow He II emission in *HST*/FOS data using a much larger aperture (K95).

Based on *IUE* spectra from 29 epochs between 1978 and 1986, W90 reported a mean contribution of O III] λ1663 to the λ1640 blend of just 16%. The higher quality mean *HST* spectrum of K95 permits us to fit the C IV λ1549 profile at the positions of He II λ1640, O III] λ1663, and O III] λλ1660.8, 1666.1, which indicates that O III] contributes about 30% of the flux in the blend. This matches well the results of the unreported line deblending analysis of K95 (see also KG00) that found a contribution of 33% in the mean *HST* spectrum. Of course, the relative contribution of O III] to the blend is likely to vary. C91 did not give an estimate of the contribution of O III] in the 1989 campaign spectra; thus, we use the two other estimates to suggest a mean He II λ1640 broad-line flux that lay between 50.3 and 60.3 for the 1989 campaign. Corrected for foreground Galactic extinction [$R = 3.1$, $E(B-V) = 0.03$, the presently accepted value from Murphy et al. 1996], this range is then 62.5–74.9.

Finally, there has been some suggestion that weak emission lines in *IUE* spectra of relatively dim sources may be found to be systematically too faint because of nonlinearity of the *IUE* detectors under low light levels (Koratkar et al. 1997). We do not know what role, if any, this played in the measurements of weak lines by C91. However, we do find it suggestive that the mean total fluxes of the two strongest lines, Lyα+Nv and C IV λ1549, changed by +1.7% and −5.5%, respectively, between the 1989 *IUE* and 1993 *HST* campaigns, while the mean total fluxes of the three weak line blends, Si IV+O IV], He II+O III], and C III]+Si III], were *all dimmer* in the *IUE* campaign— by 30.1%, 27.3%, and 23.0%, respectively. The mean λ1350 continuum was measured to be 36.7% *brighter* during the *IUE* campaign. Certainly, variability in the line strengths and ratios is expected, but the above findings seem physically implausible in regard to the weaker lines, and we suspect that indeed the He II+O III] blend was underrecorded in the 1989 *IUE* campaign spectra, perhaps by more than ∼25%. If so, then the mean broad emission line flux of He II λ1640 during the 1989 *IUE* campaign probably lay between 78.1 and 93.6.

Isolating the flux of the broad He II λ4686 line is even more problematic because of its extreme blending with Fe II and the blue wing of Hβ and possibly the so-called Wolf-Rayet lines of N III and C III near 4640 Å. He II λ4686 has never been properly isolated in the 1989 campaign spectra. D93 summed the flux inside a 177 Å wide (rest-frame) window and found a mean value of 30.0 ± 5.0 in units of 10^{-14} ergs cm^{-2} s^{-1} during the 1989 campaign. Accounting for their measured narrow-line contribution to λ4686 (1.7 ± 0.6) and rescaling the flux to the observed frame yields 27.3 ± 5.0. This uncertainty, however, does not take into account blending with other lines. Unpublished rms spectra of NGC 5548 from the 1989 and 1993 campaigns (K. Horne 2002, private communication; B. Peterson 2002, private communication; Peterson & Wandel 1999) finds very broad emission features lying near 1640 and 4686 Å, *each* with an FWHM ≈ 8500 km s^{-1} or so (W90 found similar values in their line deblending analysis). The rms spectrum readily isolates the He II lines since they apparently respond strongly to the continuum variations. The window adopted by D93 to "measure" the He II line intensity is 33% wider than these lines' apparent FWHM. Using this window, D93 also found that the amplitude of variation in the λ4686 blend is one-half that of the λ1640 blend for the same time period (C91). The discrepancy in variability amplitude was also reported in Dumont et al. (1998). It is clear that whatever else may be going on, variable contributions from Fe II and the blue wing of Hβ *could have* diluted the variability signal within the measurement window for λ4686, although of course we do not know whether contamination alone accounted for these differences. Taken together, these clues suggest that the actual contribution of broad He II λ4686 to the mean flux quoted in D93 (see also Fig. 1) plausibly lies between 45% and 67%, or 12.2 and 18.2, respectively. Accounting for foreground Galactic extinction, this range is then 13.4–20.0 in units of 10^{-14} ergs cm^{-2} s^{-1}.

Taking all of the above into consideration, we then find that the probable range in value of the mean $f(1640)/f(4686)$ ratio from the 1989 campaign is 5.1 ± 3.0, where 3.0 is the 1 σ uncertainty in the mean ratio rather than a 1 σ range in the ratio.

REFERENCES

Antonucci, R. R. J., Geller, R., Goodrich, R. W., & Miller, J. S. 1996, ApJ, 472, 502
Antonucci, R. R. J., Kinney, A. L., & Ford, H. C. 1989, ApJ, 342, 64
Baldwin, J. A. 1997, in IAU Colloquium 159, Emission Lines in Active Galaxies: New Methods and Techniques, ed. B. M. Peterson, F.-Z. Cheng, & A. Wilson (ASP Conf. Ser. 113; San Francisco: ASP), 80
Baldwin, J. A., Korista, K. T., Ferland, G. J., & Verner, D. A. 1995, ApJ, 455, L119
Blandford, R. D., & McKee, C. F. 1982, ApJ, 255, 419
Brotherton, M. S., Wills, B. J., Francis, P. J., & Steidel, C. C. 1994, ApJ, 430, 495
Clavel, J., et al. 1991, ApJ, 366, 64 (C91)
Davidson, K., & Netzer, H. 1979, Rev. Mod. Phys., 51, 715
Dietrich, M., et al. 1993, ApJ, 408, 416 (D93)
Dumont, A.-M., Collin-Souffrin, S., & Nazarova, L. 1998, A&A, 331, 11
Ferguson, J. W., & Ferland, G. J. 1997, ApJ, 479, 363
Ferguson, J. W., Korista, K. T., Verner, D. A., & Ferland, G. J. 2001, in ASP Conf. Ser. 247, Spectroscopic Challenges of Photoionized Plasmas, ed. G., J. Ferland & D. W. Savin (San Francisco: ASP), 287
Ferland, G. J. 1999, PASP, 111, 1524
———. 2002, Hazy, a Brief Introduction to Cloudy, Univ, Kentucky Physics Dept. Internal Rep.
Goad, M. R., & Koratkar, A. 1998, ApJ, 495, 718
Goad, M. R., O'Brien, P. T., & Gondhalekar, P. M. 1993, MNRAS, 263, 149
Kaspi, S., & Netzer, H. 1999, ApJ, 524, 71
Koratkar, A., Evans, I., Pesto, S., & Taylor, C. 1997, ApJ, 491, 536

Korista, K. T., Baldwin, J. A., Ferland, G. J., & Verner, D. 1997, ApJS, 108, 401
Korista, K. T., & Goad, M. R. 2000, ApJ, 536, 284 (KG00)
Korista, K. T., et al. 1995, ApJS, 97, 285 (K95)
MacAlpine, G. M. 1981, ApJ, 251, 465
MacAlpine, G. M., Davidson, K., Gull, T., & Wu, C.-C. 1985, ApJ, 294, 147
Maoz, D., et al. 1993, ApJ, 404, 576
Murphy, E. M., Lockman, F. J., Laor, A., & Elvis, M. 1996, ApJS, 105, 369
Netzer, H., & Laor, A. 1993, ApJ, 404, L51
O'Brien, P. T., Goad, M. R., & Gondhalekar, P. M. 1994, MNRAS, 268, 845
———. 1995, MNRAS, 275, 1125
O'Brien, P. T., et al. 1998, ApJ, 509, 163
Osterbrock, D. 1989, Astrophysics Of Gaseous Nebulae and Active Galactic Nuclei (Mill Valley: University Science Books)
Peterson, B. M. 1993, PASP, 105, 247
———. 2001, in ASP Conf. Ser. 224, Probing the Physics of Active Galactic Nuclei, ed. B. M. Peterson, R. W. Pogge, & R. S. Polidan (San Francisco: ASP), 1
Peterson, B. M., & Wandel, A. 1999, ApJ, 521, L95
Rees, M., Netzer, H., & Ferland, G. J. 1989, ApJ, 347, 640
Reichert, G., et al. 1994, ApJ, 425, 582
Rodriguez-Pascual, P. M., et al. 1997, ApJS, 110, 9
Storey, P. J., & Hummer, D. G. 1995, MNRAS, 272, 41
Wamsteker, et al. 1990, ApJ, 354, 446 (W90)
Wanders, I., et al. 1997, ApJS, 113, 69
Weymann, R. J., & Williams, R. E. 1969, ApJ, 157, 1201